Journal of Alloys and Compounds 857 (2021) 157561

Contents lists available at ScienceDirect

Journal of Alloys and Compounds

journal homepage: http://www.elsevier.com/locate/jalcom

Effect of silver addition in copper-silver alloys fabricated by laser powder bed fusion in situ alloying

John Robinson [a, b, *], Arun Arjunan [a], Mark Stanford [b], Iain Lyall [a], Craig Williams [a]

[a] School of Engineering, University of Wolverhampton, Telford Innovation Campus, Telford, TF2 9NT, UK
[b] 6DME Ltd., Stirchley Road, Telford, TF3 1EB, UK

ARTICLE INFO

Article history:
Received 23 April 2020
Received in revised form
9 October 2020
Accepted 11 October 2020
Available online 16 October 2020

Keywords:
Additive manufacturing
Selective laser melting
CuAg
In situ
Computed tomography
X-ray diffraction
Atomic lattice structure

ABSTRACT

In this study copper-silver (CuAg) structures with varying Ag content were fabricated by in situ alloying and Laser Powder Bed Fusion (L-PBF) Additive Manufacturing (AM). Powder morphology, distribution and elemental analysis were conducted using Scanning Electron Microscopy (SEM) and dynamic imaging for CuAg10, CuAg20 and CuAg30 atomised powder. The resultant pore defect morphology and distribution for each as built and annealed CuAg alloy structure was investigated and reported using X-ray Computed Tomography (XCT) and 3D visualisation. The atomic crystal structure for each as built and annealed CuAg alloy is reported through X-Ray Diffraction (XRD) analysis. Yield strength, Young's Modulus, failure strain and Ultimate Tensile Strength (UTS) of as built and annealed AM CuAg structures are reported and sample fracture surfaces were analysed using SEM and Energy Dispersive X-Ray (EDX) techniques. Increased Ag content from CuAg10% to CuAg30% is shown to decrease the number of pore defects by 87% and 83% for as built and annealed samples with average pore size decreasing by 40% and 9.5%. However, the annealing process was found to increase the porosity by up to 164%. Furthermore, the annealing process resulted in atomic lattice contractions resulting in increased yield strength, Youngs Modulus and Ultimate Tensile Strength (UTS) for CuAg30%.

1. Introduction

Silver (Ag) and copper (Cu) are highly reflective materials with desirable antimicrobial, thermal and electrical conductive properties [1–5] and as such these materials are of interest for a wide range of applications such as renewable energy, biomedical, electronics and thermal management [3,4,6–8]. Ag is usually utilised as an alloying element [9–11], however, research has shown that increasing Ag addition by as little as 2 and 3% can increase thermal conductivity and diffusivity as well as hardness and compressive strength of aluminium-copper-silver (AlCuAg) alloys [12]. A 10% increase of Ag in titanium-silver (TiAg) alloy lowered the compressive stress by 80% and hardness by 30% [7] while Ag addition between 0.5% and 2% in molybdenum-copper-silver (MoCuAg) alloys increased electrical and thermal conductivity with negligible effect on the Coefficient of Thermal Expansion (CTE) [8].

Although the studies mentioned highlight the potential benefits of CuAg alloys, the powder metallurgy associated with manufacturing techniques utilised for alloy fabrication are limited with little research conducted on advanced manufacturing technologies such as Additive Manufacturing (AM). Cu and its alloys are gaining popularity due to relatively lower material cost and as such are undergoing research utilising AM techniques such as Laser Powder Bed Fusion (L-PBF) [13–17]. During the L-PBF process 3D components are fabricated by Selective Laser Melting (SLM) a 2D layer on preceding layer. L-PBF is capable of creating improved material properties in comparison to conventional manufacturing techniques such as casting [18] and fabricating complex 3D geometries unfeasible with traditional manufacturing techniques [19–21]. Therefore the creation of complex metallic alloys and Metal Matrix Composite (MMC) materials and structures are being increasingly reported [20,22–24]. Furthermore, L-PBF in situ alloying has been shown to be a feasible manufacturing technique resulting in desirable material performance for various alloys [25–27].

For example, studies investigating L-PBF in situ alloying of titanium-tantalum (TiTa), aluminium-copper (AlCu) and

* Corresponding author. School of Engineering, University of Wolverhampton Telford Innovation Campus, Telford, TF2 9NT, UK.
E-mail addresses: john@6dme.com, j.robinson12@wlv.ac.uk (J. Robinson).

https://doi.org/10.1016/j.jallcom.2020.157561
0925-8388/

aluminium-silicon (AlSi) have recently been reported. Huang et al. [28] utilised L-PBF to fabricate TiTa alloys with 0, 10, 30 and 50% Ta content and investigated the resultant mechanical and biocompatibility properties. Ti50Ta was shown to be biocompatible however as built samples displayed randomly dispersed Ta particles in a TiTa matrix with unmolten Ta particles visible by optical microscopy. Although difficult to process due to reflective and thermal conductive properties Martinez et al. [29] successfully fabricated AlCu alloys through L-PBF in situ alloying and reported the resultant mechanical performance. Samples displayed homogenous microstructures consisting of an Al rich matrix and mechanical performance was shown to be comparable to more traditionally manufactured samples. However, while the studies discussed highlight the potential of L-PBF in situ alloying of difficult to process thermally conductive materials the L-PBF in situ alloying of Ag and Cu with relatively large Ag content has yet to be reported. Furthermore, the SLM process has over 130 variables including the feedstock and process [30] and these include material absorptivity and reflectivity, laser diffusion and scattering, heat transfer and material phase transformation [31] and L-PBF material feedstock properties such as apparent density, particle distribution and powder flowability can have a significant effect on powder layer delivery and the creation of porosity defects. Therefore, the SLM processing of reflective and thermally conductive materials such as Ag and Cu can be difficult [2,32,33] with some studies reporting maximum pure Cu densities of 85.8% utilising L-PBF [2]. Subsequently Ag and Cu are usually utilised as alloying elements to exploit their desired properties [34,35]. In addition the laser and material interaction and selected process parameters and scanning strategy can result in lack of fusion, keyhole and blowhole defects for alloys and MMC's [36,37]. Pore defects produced during the L-PBF process have seen increasing investigation [36,38,39] and are characterised to be either lack of fusion, keyhole and blowhole defects [36]. Keyhole and blowhole pore defects are spherical in shape and are caused by trapped gas while lack of fusion porosity appear as larger irregular shaped pores [36]. These can be caused by insufficient powder delivery and/or insufficient energy at the powder bed. Furthermore, powder morphology as well as unoptimised parameters could result in pore defect generation and material failure. For example previous studies on the L-PBF of pure silver have shown material failure at lack of fusion porosity sites with the unmolten powder particles visible at fracture surfaces [40].

While the L-PBF of Ag and Cu as alloying and base elements is undergoing increasing research, the morphology and distribution of porosity throughout L-PBF CuAg fabricated structures are yet to be understood. Understanding this aspect is critical for the development of novel alloys as pore defects have a significant effect on the thermomechanical properties [41,42] of the components. Therefore, understanding L-PBF pore defect distribution for CuAg structures will aid in their optimum fabrication for a variety of industries and applications. Accordingly, this study reports the L-PBF fabrication of CuAg10, CuAg20 and CuAg30 alloys and their resultant mechanical performances both as built and annealed. L-PBF powder composition, morphology and distribution are reported using dynamic imaging, Scanning Electron Microscopy (SEM) and Energy Dispersive X-Ray (EDX) analysis. Fabricated pore defect morphology and distribution are described through X-ray Computed Tomography (XCT) 3D visualisation and CuAg alloy crystal structure is analysed through X-Ray Diffraction (XRD) techniques. Yield strength, Young's Modulus, failure strain and Ultimate Tensile Strength (UTS) of as built and annealed CuAg structures are reported and sample fracture surfaces are analysed using SEM and Energy Dispersive X-Ray (EDX). This research offers an insight into the mechanical properties and pore defect morphology and distribution in L-PBF SLM highly reflective and thermally conductive CuAg structures with varying Ag content.

2. Material and methods

The L-PBF investigations presented in this study were carried out on an EOS M290 industrial grade AM system using CuAg10%, CuAg20% and CuAg30% powders comprising of atomised pure Cu and Ag powders. The L-PBF system featured a 400W laser with 100 μm spot size and all builds were completed in an argon atmosphere with oxygen content in the process chamber below 0.1%. The process was carried out on substrates heated to 35 °C. Following fabrication all samples were removed from the build platform using none contact Electrical Discharge Machining (EDM) techniques. Half of the as built samples were post heat treated with a CuAg annealing process and subsequent mechanical testing was conducted using a Zwick Roell 1474 material test system with 100 kN maximum load capacity. A Bruker Skyscan 2211 X-ray nanotomograph was used to analyse sample pore defect distribution and morphology while fracture surfaces were analysed using Scanning Electron Microscopy (SEM). Atomic lattice structure analysis was conducted using Panalytical Empyrean, copper anode X-Ray Diffraction system operating at 40 KV and 40 mA. XRD was selected for this study as it offers data analysis over a relatively larger area in comparison to other more focused analysis techniques which is beneficial for the first reported analysis of L-PBF CuAg alloy structures.

2.1. Powder characterisation

Powder morphology and particle distribution can affect the packing density and flowability of AM powders [43] and therefore dictate the thermomechanical behaviour during the AM process [43]. Atomised CuAg powder combinations utilised in this study were created using pure Cu and Ag powders proven to be suitable for L-PBF processing in previous studies [40]. Pure Ag powder displayed a larger distribution of powder particles below 20 μm with visible satellite particles while pure Cu powder particles displayed a larger distribution above 20 μm with fine particles also visible. However, both pure Cu and Ag displayed an evenly distributed particle size and relatively spherical powder morphology which is desired for the L-PBF process to enhance both the packing density and the flowability of the powder [43]. Pure Ag was shown to have a PVD of D_{10} of 20.3 μm, D_{50} of 30.2 μm and D_{90} of 41.4 μm while pure Cu featured a PVD of D_{10} of 44.0 μm, D_{50} of 52.1 μm and D_{90} of 58.2 μm. As a D_{90} of 10 μm can result in unusable powder for L-PBF processing [44], the pure Cu and Ag are suitable for L-PBF AM. Energy Dispersive X-Ray Spectroscopy (EDX) analysis was completed using a Zeiss EVO50 SEM to confirm the elemental content of pure Cu and pure Ag powders before mixing. Pure Cu and Ag powders were shown to be 99.08% (Cu) and 99.73% (Ag) respectively with balance oxygen. To confirm homogenous distribution the element content, morphology and Particle Size Distribution (PSD) of the CuAg powders were characterised using SEM and digital particle analysis techniques. A Retsch Technology Camsizer x2 was used to analyse particle distribution. The resulting SEM data for CuAg powders are shown in Fig. 1. CuAg powder particles can be seen to be spherical in shape, however, the morphology and Particle Size Distribution (PSD) varies with Ag content due to the differences in Cu and Ag morphology. Cu particles are generally larger with a mix of smaller Cu and Ag powder particles within the powder samples.

To confirm the element content of the powders, Energy Dispersive X-Ray (EDX) analysis was conducted using a Zeiss EVO50 SEM. Fig. 2 shows the EDX spectra data with Table 1 showing the

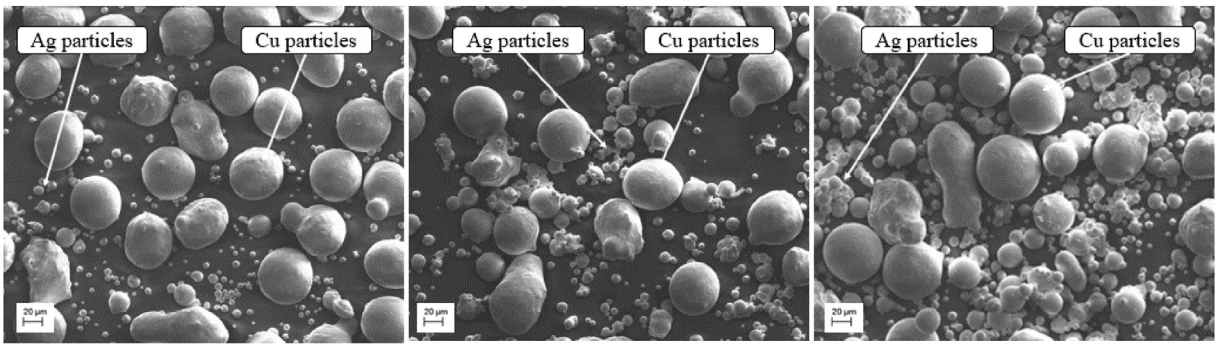

Fig. 1. Scanning Electron Microscopy (SEM) images for CuAg powders showing (a) CuAg10, (b) CuAg20 and (c) CuAg30.

elemental composition for each of the CuAg powder mixes highlighting that the respective increase in Ag content as expected with the respective 10, 20 and 30% addition.

Although the content of Ag increases as anticipated with expected elemental compositions, the actual weight % for each CuAg powder mix varies. This could be due to non-homogenous distribution within the powder mix or variations in the EDX results due to powders nonuniform morphology. To establish excessively high or low particle distribution that can affect the powders processability for L-PBF AM the CuAg powders D_{10}, D_{50}, and D_{90} vol fractions were identified. Particle Volume Distribution (PVD) and corresponding D_{10}, D_{50}, and D_{90} for each CuAg alloy are shown in Fig. 3. D_{10} vol decreases as Ag content increases due to pure Ag lower PSD. D_{50} and D_{90} vol remain relatively unchanged for all CuAg powder mixes. A D_{90} of 10 μm can result in unusable powder for L-PBF processing [44] and therefore the PVD values shown in Fig. 3 suggest that the CuAg powders measured in this study are suitable for L-PBF AM.

2.2. Annealing process

L-PBF CuAg alloys have seen limited investigations, in any case compositions with a relatively high Ag content alloys of 10%, 20% and 30% have not been investigated to date. However, cast CuAg alloys with high compositions have been investigated. Shannon et al. [45] studied ingot cast CuAg alloys at compositions including CuAg30, CuAg20 and CuAg5 and reported the recrystallisation and optimum annealing process. For cast and work hardened CuAg alloys the investigations determined the recrystallisation temperature for CuAg30 to be 500 °C for a 30 min anneal time. During annealing the internal residual stresses introduced by the work hardening were shown to be relieved without change in strength or hardness [45]. Although not work hardened, the L-PBF process is known to create internal stresses within fabricated components due to the rapid heating and cooling cycles associated with the SLM process [46,47]. Accordingly, to investigate post heat treatment and recrystallisation for L-PBF CuAg alloys, 50% of the as built samples were annealed at 500 °C for a 30 min period and left to cool. Atomic lattice structure variations were then investigated using X-Ray Diffraction (XRD) and the results reported alongside the resultant effects on mechanical performance and pore defect distribution.

3. Results and discussion

3.1. Additively manufactured test coupons

SLM process parameters developed in previous studies were used for initial CuAg sample fabrication and are displayed in Table 2 while as built CuAg10, CuAg20 and CuAg30 samples are shown in Fig. 4. While it is known varying L-PBF process parameter sets can affect the resultant material performance [48], processing parameters were kept constant for this study to ensure material performance variations were related to material composition and Ag content. Although all CuAg samples were fabricated with the same parameters and had visibly similar surface finish there was a clear colour variation throughout due to the increased Ag content, particularly with the higher Ag 30% content (Fig. 4c).

3.2. Density and pore defect analysis

Understanding L-PBF porosity morphology and distribution is crucial for understanding the effects of L-PBF processing and material failure. While industrial grinding and polishing techniques combined with SEM imaging can supply an indication of fabricated component density and defect content, they offer limited information on distribution throughout the sample due to only supplying a result of 2D data. Accordingly, X-Ray Computed Tomography (XCT) analysis was conducted to ascertain a 3D visualisation of porosity morphology and distribution and to investigate any resultant pore defect variations associated with increased Ag addition.

XCT is a nondestructive analysis technique, which can be used for AM pore defect analysis [42,49]. Incorrect powder feedstock properties such as PVD and poor flowability can lead to nonuniform powder layer delivery and porosity defects. However pore defects can also result from laser and material interaction and process and scanning strategy parameters [36]. XCT analysis for this study was conducted utilising a Bruker Skyscan 2211 X-ray nanotomograph. While XCT sample analysis is a valuable tool for nondestructive pore defect analysis, the results achieved are dependent on the scanning and threshold parameters set by the operator. Therefore, XCT techniques are better utilised for comparative rather than absolute analysis. Comparative analysis ensures XCT scanning and threshold parameters are kept constant and therefore any variations in density and porosity defects can be attributed to AM feedstock material, process parameters used for manufacturing or post processing techniques such as annealing. For this reason, all samples were scanned with the same XCT scanning, threshold and reconstruction parameters to ensure any notable changes in porosity can be attributed to either the difference of Ag in the AM material feedstock or the annealing process. XCT porosity data for L-PBF CuAg alloys at Ag 10%, 20% and 30% are shown in Fig. 5. The number of pores and average pore size was found to decrease as Ag content increases for both CuAg as built and annealed samples. Overall, the quantity of pores decreased by 87% and 83% while

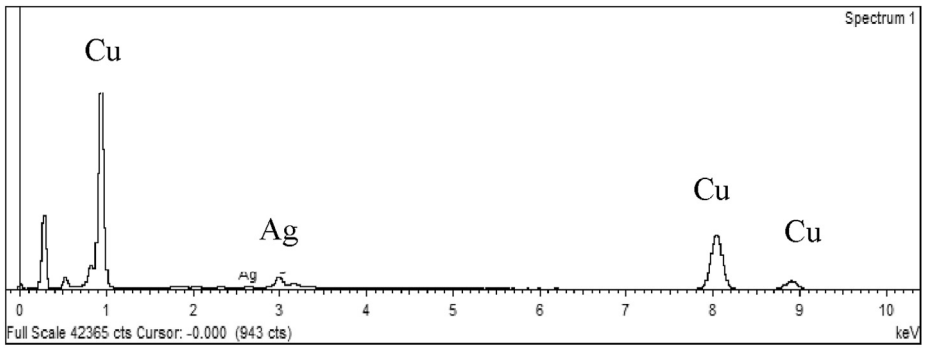

(a)

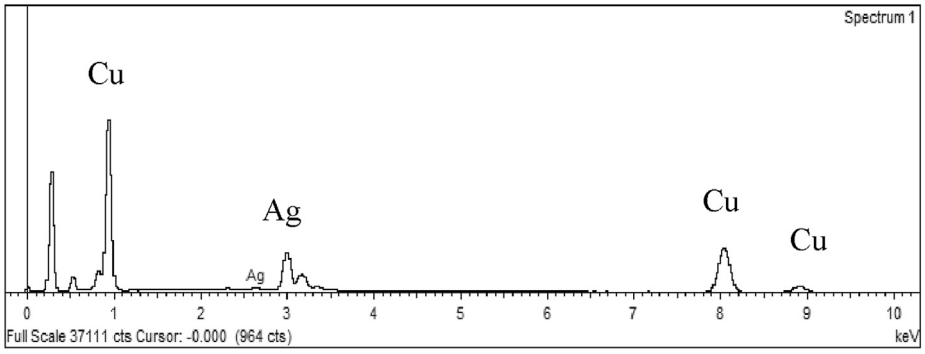

(b)

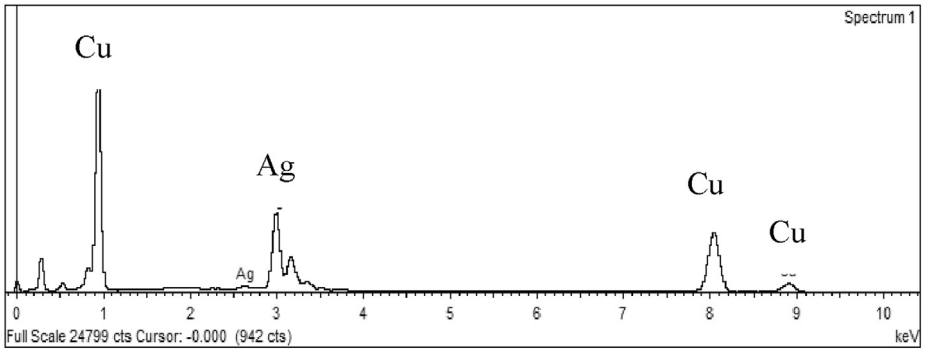

(c)

Fig. 2. Energy Dispersive X-Ray (EDX) element spectra for (a) CuAg10, (b) CuAg20 and (c) CuAg30.

Table 1
Elemental weight composition of the different CuAg mixtures as informed by the EDX spectrum.

Material	Element	Weight (%)
CuAg10	Cu	92.51
	Ag	07.49
CuAg20	Cu	72.50
	Ag	27.50
CuAg30	Cu	64.20
	Ag	35.80

average pore size decreased by 40% and 9.5% for as built and annealed samples respectively.

The annealed samples display a larger proportion of pores and larger average pore size clearly showing the annealing process increases pores content, particularly at lower (10%) Ag content, which showed a 164% increase between as built CuAg10 as built sample to annealed CuAg10 sample. Furthermore, the annealing process can be seen to increase pore defect content with corresponding samples displaying either similar or higher number of pores and average pore sizes in 11 out of the 12 cases.

X-ray absorption rates varied for both as built and annealed CuAg samples as shown in Fig. 6a–c and Fig. 7a–c respectively. High X-ray absorption signifies a relatively dense material as identified by 1 (blue), on the contrary 0 (black) represents areas of lowest X-Ray absorption and therefore potential voids (absence of

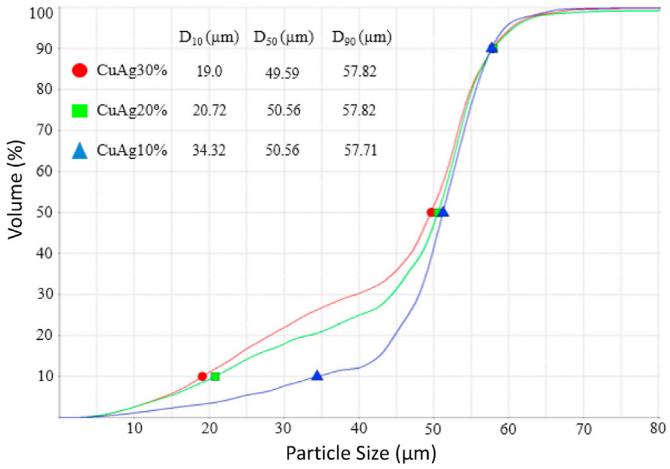

Fig. 3. Particle Volume Distribution (PVD) for CuAg10, CuAg20 and CuAg30 powders.

material). To analyse the pore defect morphology and distribution throughout the samples the internal closed pore porosity voids were isolated for as built and annealed samples as shown in Figs. 6c and 7c respectively. Higher Ag content was found to correspond with less pore defects for both as built (Fig. 6) and annealed (Fig. 7) samples, however as built samples displayed significantly lower pore defects (Fig. 6) in comparison to annealed samples (Fig. 7). The XCT data and 3D visualisations seen in Figs. 6 and 7 show clear variation in the number of pores and average pore size as Ag content increases. The addition of Ag reduces pore content and average pore size significantly while annealing increased pore content and pore size for all CuAg compositions. CuAg30 with the largest Ag content was found to have the lowest pore defect content for both as built (Fig. 6) and annealed (Fig. 7) samples.

Pore defects have been shown to negatively affect a materials mechanical performance [39,40,50] and therefore the larger content of these defects seen in the annealed and lower Ag content samples would expect to exhibit lower mechanical strength. Reduced porosity due to increased Ag content could be due to lower powder PVD resulting in improved packing density and layer delivery or atomic bonding in the CuAg alloy system. Accordingly, atomic lattice structure was investigated utilsing X-Ray Diffraction (XRD) techniques.

3.3. Influence on crystal structure

Pure Cu and Ag with face centered cubic (fcc) atomic lattice structures [3,51] but varying atomic size differences result in relatively large lattice mismatches in the CuAg alloy system [3,52]. However, at ∝12% the CuAg system still conforms to the Hume−Rothery criteria for fcc metals, with atomic size differences within 15% [51,52]. Therefore, the CuAg system is of significant interest and as such has seen investigations relating to alloying behavior, atomic vacancy effects, miscibility, phase stability and recrystallisation [45,52−54] utilising atomistic and molecular dynamic simulations, electrodepositing, casting and XRD [3,45,51,53,55]. Despite this L-PBF CuAg alloy crystal lattice structures at relatively high Ag content (Ag10%, Ag20% and Ag30%) have not seen investigation. Accordingly, L-PBF CuAg alloy lattice structures and atomic d-spacing were investigated using a Panalytical Empyrean, copper anode X-Ray Diffraction system operating at 40 KV and 40 mA.

The XRD cluster analysis as shown in Fig. 8 was carried out to identify any variations between CuAg structures at an atomic level with L-PBF pure Cu used as a reference sample. Using the eigenvector mathematical procedure, a smaller data set is created, and data variables are collated into corresponding groups or principal components. Although using a reduced data set, cluster analysis allows for XRD data visualisation highlighting data variances and similarities [56] and displaying them within related coloured spheres. Fig. 8 clearly demonstrates separation and variation in atomic structure for L-PBF pure Cu and as built and annealed CuAg alloy samples. The addition of Ag and the annealing process have obvious effects at the atomic level. The annealing process can be seen to create a similar atomic structure for annealed samples due

Table 2
SLM process parameters used for CuAg alloy fabrication.

Parameter	Laser Power (W)	Scan Speed (mm/s)	Hatch Distance (mm)	Layer Thickness (μm)
Values	370	400	0.14	30

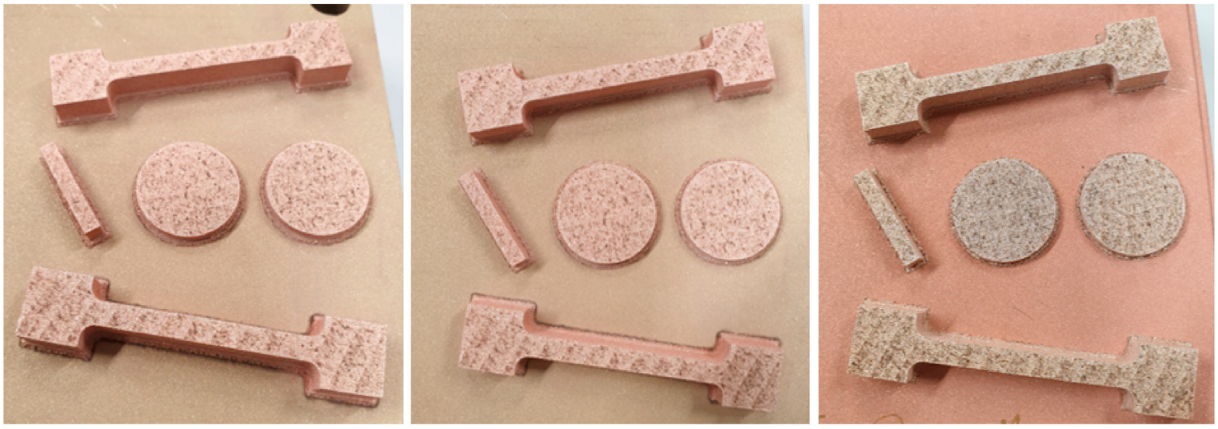

Fig. 4. As built CuAg in situ alloy samples on build substrates showing (a) CuAg10, (b) CuAg20 and (c) CuAg30.

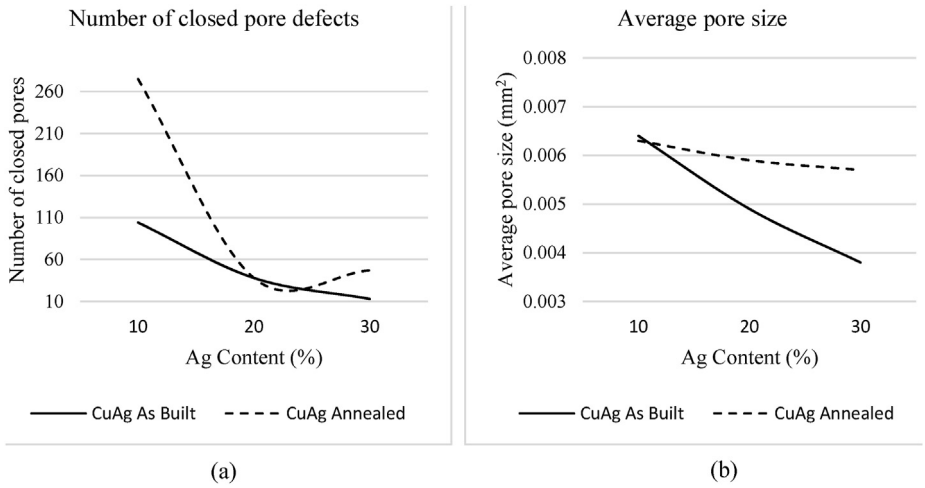

Fig. 5. XCT pore defect data for SLM CuAg alloys as built and annealed showing (a) number of closed pore defects and (b) average closed pore size.

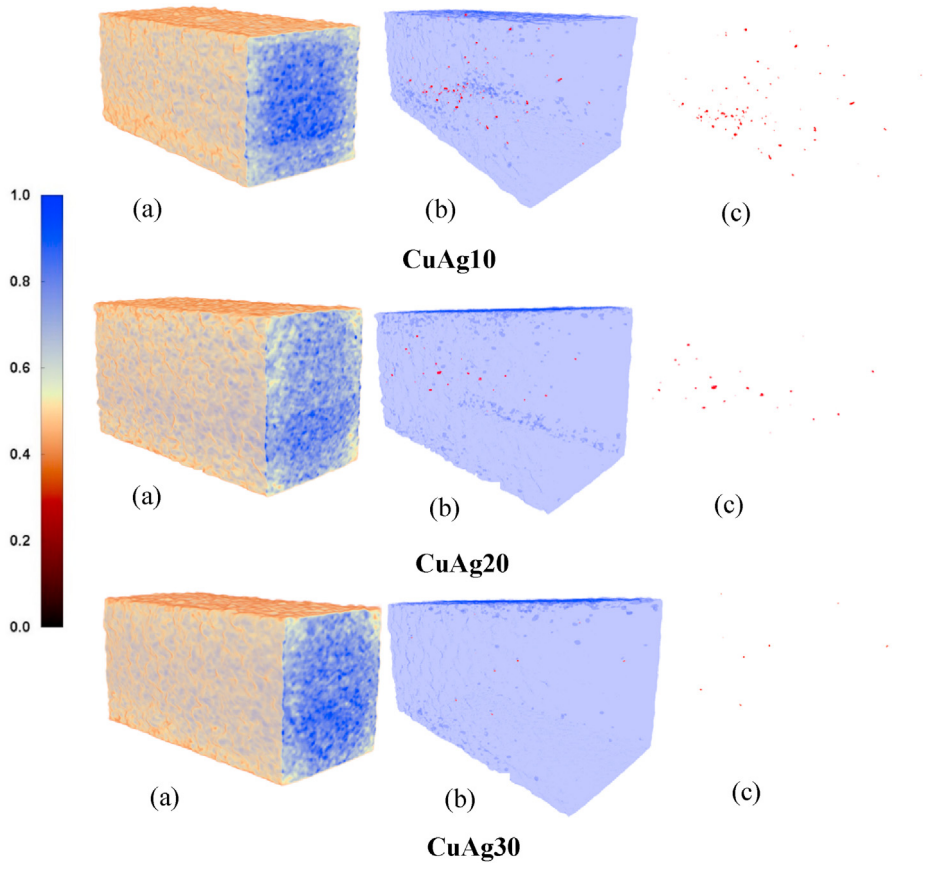

Fig. 6. X-ray computed tomography 3D visualisation of as build CuAg samples under different compositions as identified showing (a) complete sample, (b) highlighted porosity within the sample and (c) internal closed pores isolated for clarity.

to recrystallisation with all annealed samples clustered in proximity. As built samples also display similar atomic structure to each other however cluster analysis shows there is more variance.

The cluster analysis displays clear variations in atomic lattice structure between annealed samples and as built (none heat-treated) samples and therefore XRD data for pure Cu and all CuAg samples was investigated further to investigate atomic lattice variations. L-PBF pure Cu was used as reference sample and the XRD spectrum data was obtained for pure Cu as shown in Fig. 9. Pure Cu peaks appeared at 2 Theta = 43.2°, 50.3° and 74.2° respectively, which is consistent with fcc Cu JCPDS (Joint Committee on Powder Diffraction Standard) cards.

XRD spectrum data for CuAg alloys as built and annealed can be seen in Figs. 10–12. New Ag peaks are present, which increased in count and height as Ag composition content increased from 10% to 20% and 30%. This confirmed the homogenous distribution of Ag

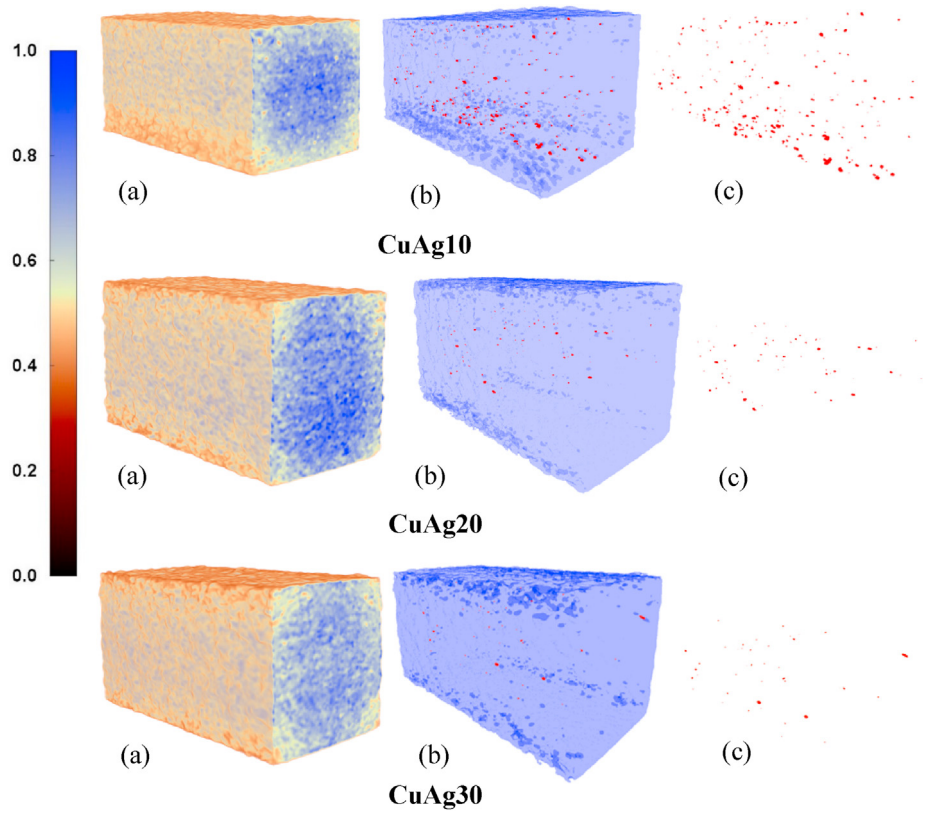

Fig. 7. X-ray computed tomography 3D visualisation of annealed CuAg samples under different compositions as identified showing (a) complete sample, (b) highlighted porosity within the sample and (c) internal closed pores isolated for clarity.

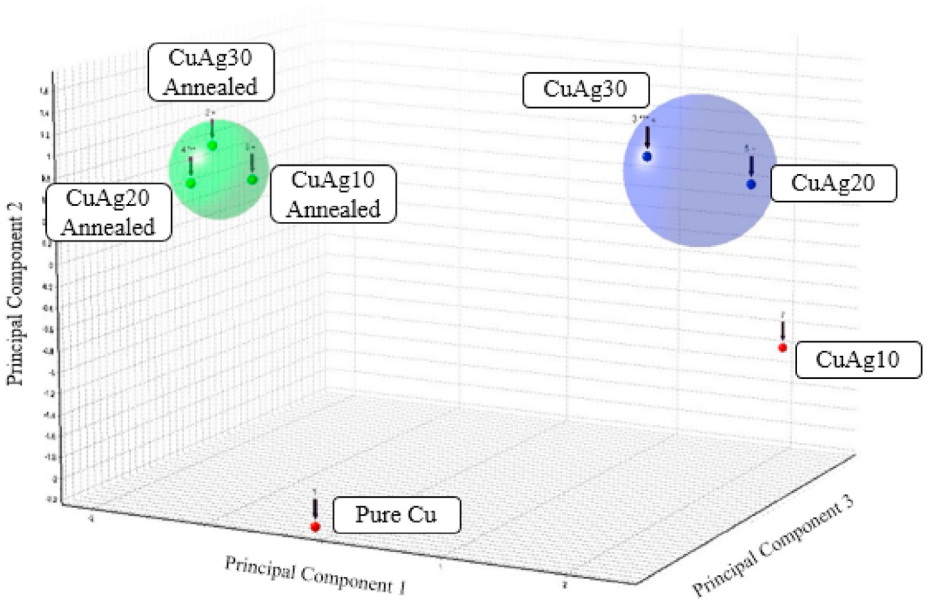

Fig. 8. X-Ray Diffraction (XRD) cluster analysis for SLM pure Cu and as built and annealed CuAg alloys.

throughout all CuAg samples which all also displayed cubic atomic structures. Furthermore, all samples saw 2° Theta values decrease (Fig. 13a) with increased Ag content suggesting an increase in d-spacing (Fig. 13b) which is explained by the presence of the relatively larger silver atoms within the CuAg atomic lattice structures.

However, following the annealing process d-spacing saw significant reductions in relation to as built samples (Fig. 13b) due to the recrystallisation and contraction of atomic lattice structures. This atomic lattice contraction therefore explains the increase in pore defects seen in XCT 3D visualisation (Figs. 6 and 7). As atomic lattice contractions occur, number of pores and the average size increase where voids are present throughout the CuAg samples. D-

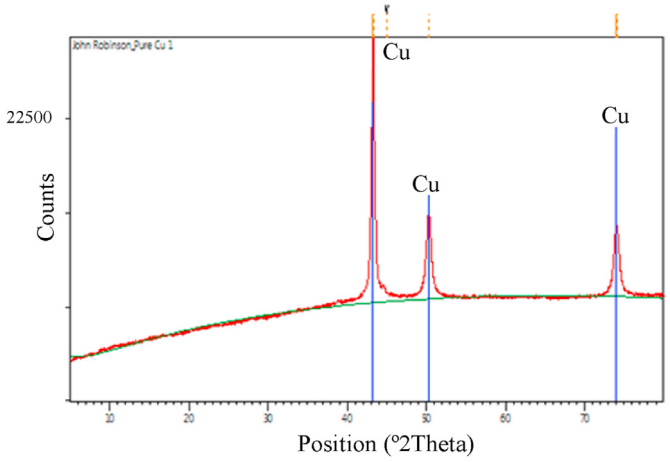

Fig. 9. XRD spectra data for SLM pure Cu.

spacing reduced by 0.29%, 1.29% and 2.26% respectively for CuAg10, CuAg20 and CuAg30 following the annealing process. As built d-spacing displayed a 1.93% increase with increased Ag content from CuAg10 to CuAg30 while annealed samples saw a maximum 0.2% change in d-spacing for all three samples. Furthermore, annealed samples exhibited d-spacing values below that of as built L-PBF pure Cu.

3.4. Mechanical performance

The addition of Ag to Cu has seen significant research [4,57] and has been shown to have strengthening effects due to fine dendrites and an increase in CuAg phase boundaries, which have a strong binding effect. Furthermore, Cu matrix and CuAg interfaces were shown to hinder dislocation movements [58]. However, investigations regarding the interaction between Cu and Ag at an atomic level for L-PBF CuAg alloys has not been investigated. Accordingly, Fig. 14 presents the stress-strain ($\sigma - \varepsilon$) curve for L-PBF CuAg10, CuAg20 and CuAg30 alloys with the corresponding performance parameters such as the Yield strength (σ_y), Youngs Modulus (E), failure strain (ε_f) and Ultimate Tensile Strength (UTS) values shown in Fig. 15.

The $\sigma - \varepsilon$ data clearly displays an increase in E (Fig. 15b), σ_y (Fig. 15a) and UTS (Fig. 15d) with increased Ag addition for both as built and annealed samples with the highest E, σ_y and UTS displayed with Ag 30% for all samples. As built samples showed an increase in σ_y of 23% and 48% as Ag content increased from 10% to 20% and 30% while annealed samples saw σ_y increase by 36% and 87% respectively (Fig. 16a). Similarly, UTS as built samples saw increases of 22% and 37% while UTS annealed samples increased by 31% and 68% (Fig. 16 b). With σ_y and UTS increases of 87% and 68% for Ag addition at 30% it is clear the annealing process has a more profound effect on material strength with higher Ag addition above 20%. While as built CuAg10 samples display higher E, σ_y and UTS than the equivalent CuAg10 annealed samples. The

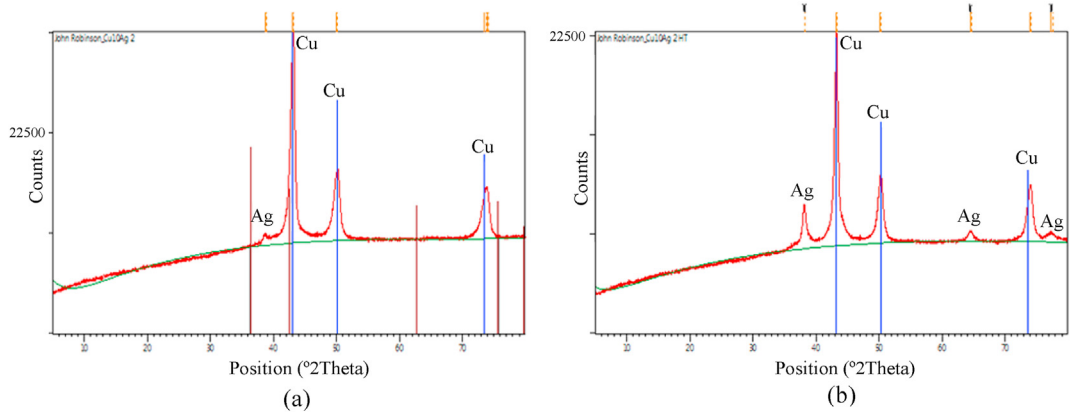

Fig. 10. XRD spectra data for (a) CuAg10 as built and (b) CuAg10 annealed.

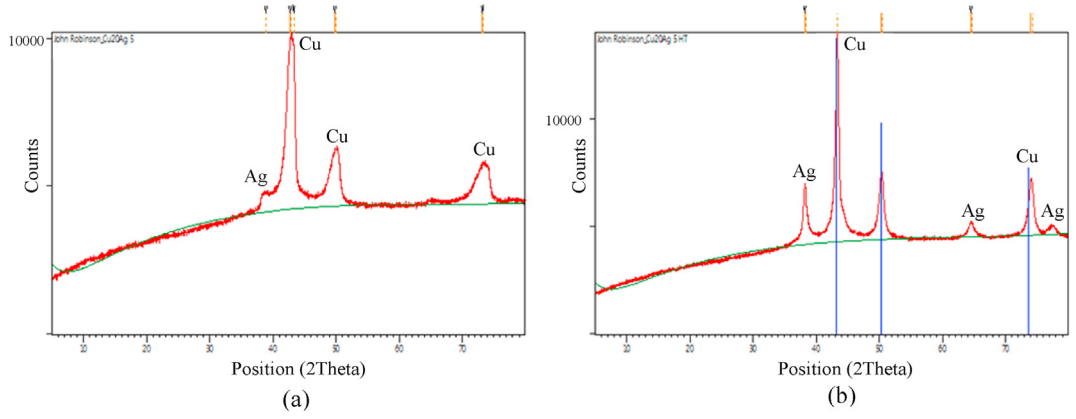

Fig. 11. XRD spectra data for (a) CuAg20 as built and (b) CuAg20 annealed.

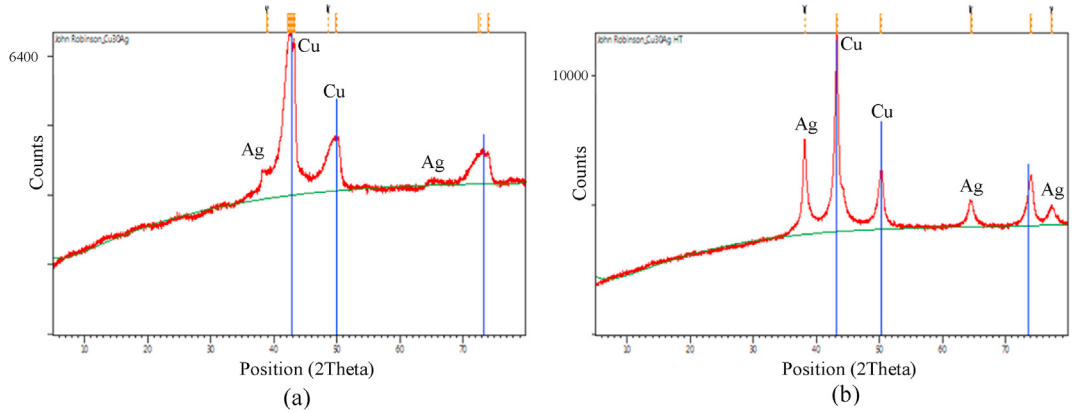

Fig. 12. XRD spectra data for (a) CuAg30 as built and (b) CuAg30 annealed,

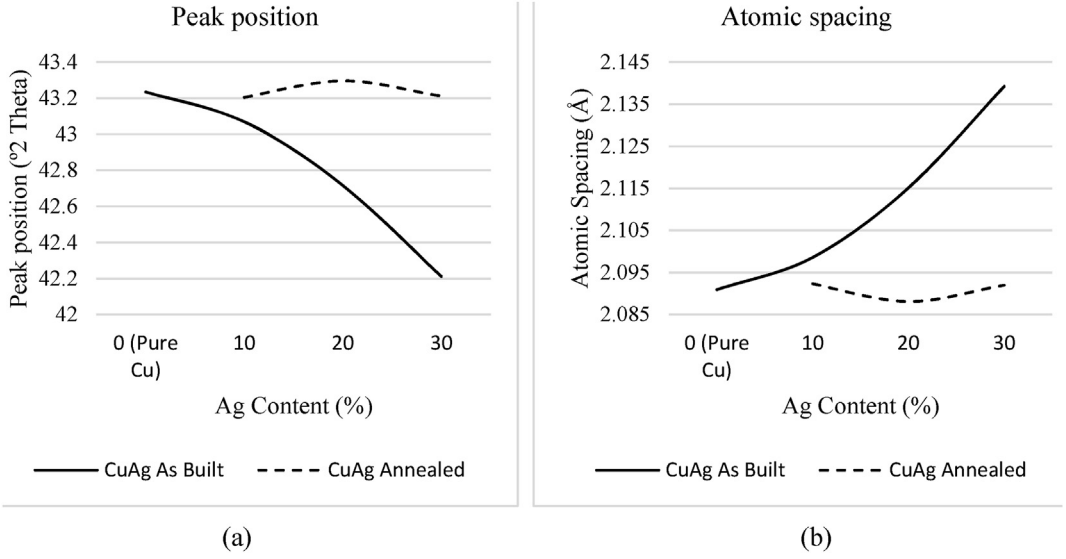

Fig. 13. XRD data for CuAg in situ alloys showing (a) peak position and (b) atomic d-spacing.

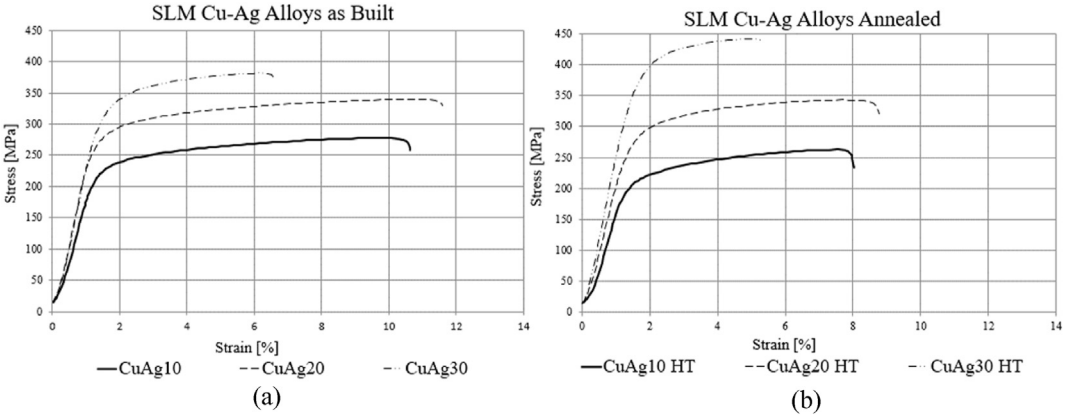

Fig. 14. Engineering Stress-strain curves for SLM CuAg alloy samples for (a) as built and (b) annealed.

CuAg20 samples whether as built or annealed have comparable σ_y and UTS values. The results confirm that the Ag addition does create an increase in mechanical performance within L-PBF CuAg alloys. Furthermore, Ag addition increased E which saw increases of 23% and 15% for as built samples and 15% and 36% for annealed samples.

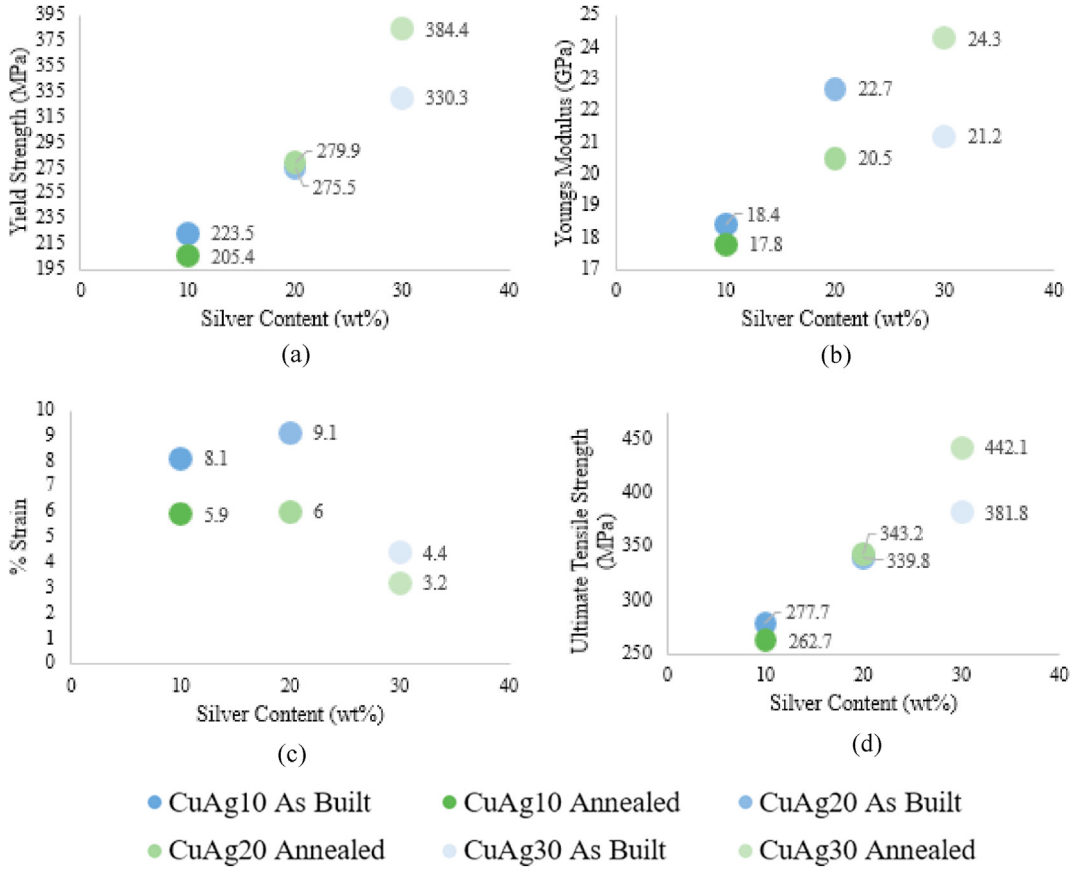

Fig. 15. Influence of Ag content and annealing on the mechanical performance of SLM CuAg alloys showing (a) yield strength, (b) Young's Modulus, (c) failure strain and (d) ultimate tensile strength.

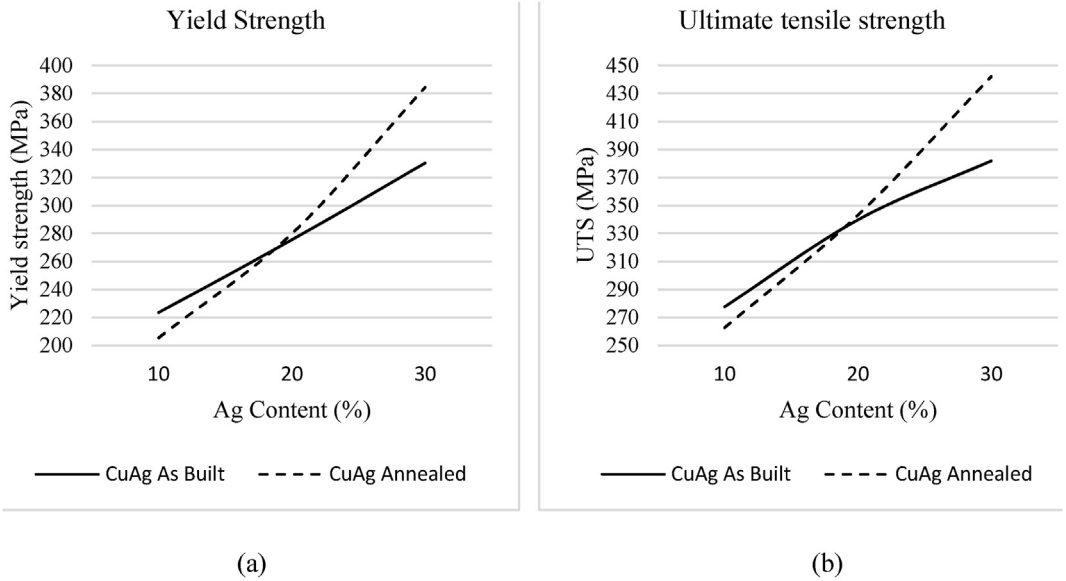

Fig. 16. Influence of Ag content and annealing process on the mechanical performance of SLM CuAg alloys showing (a) yield strength and (b) ultimate tensile strength.

Effects of Ag addition on ε_f was less obvious with CuAg20 displaying the largest ε_f values for both as built and annealed samples. However, ε_f was seen to reduce for all samples (Figs. 15c and 17a) following annealing due to recrystallisation and atomic lattice contraction resulting in stronger binding effect on CuAg interfaces reducing dislocation movements which also increased E (Fig. 17b).

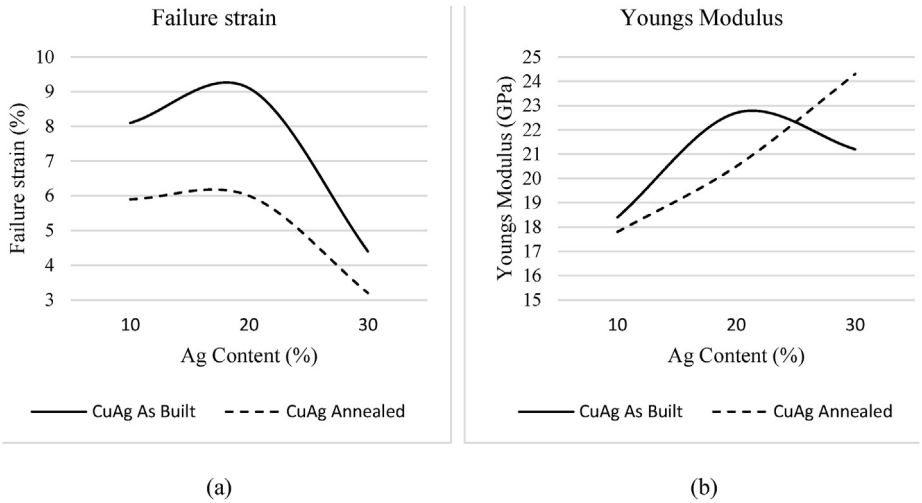

Fig. 17. Influence of Ag content and annealing process on the mechanical performance of SLM CuAg alloys showing (a) failure strain and, (b) Young's modulus.

3.5. Fractography

SEM data for SLM CuAg fracture surfaces are shown in Figs. 18–20. Although none of the CuAg fracture surfaces exhibited unmolten powder particles expected at lack of fusion pore sites some porosity voids are clearly visible as confirmed by the XCT data. The cross-section of the fracture surface shows a specific pattern where dimples of various size, shape, and distribution can be observed. Failure can be seen to be dominated by the growth of coarse voids between dimpled peaks consecutively being strained to failure.

To ascertain pore defect content at each CuAg fracture surface Olympus Stream Essentials software was utilised for comparative porosity analysis. Results (Fig. 21) concluded pore content at the fracture site decreases with Ag addition for both as built and annealed samples while porosity content values were higher for all annealed samples in comparison to as built structures confirming the XCT data results (Fig. 5a and b).

To confirm homogenous element distribution throughout the CuAg structures, EDX analysis was conducted on each fracture surface and compared with EDX elemental content of the CuAg powder. Spectrum analysis (Fig. 22) confirms increase in Ag content at the sample fracture surface as can be seen from the data in Table 3. While CuAg10 Ag fracture content differed from CuAg10 Ag powder content both CuAg20 and CuAg30 Ag content for powder and fracture surfaces was shown to be comparable. Although EDX analysis highlights some variations the Ag content throughout all fabricated CuAg structures was relatively close to the initial Ag powder composition confirming a relatively homogeneous distribution throughout powder and in situ alloyed structures.

4. Future research

The L-PBF in situ alloying of varying Ag content CuAg structures reported in this study highlight the feasibility of L-PBF in situ alloying of highly reflective and thermally conductive Cu and Ag materials and resultant mechanical performance. The aim is that this data will act as a start point for custom alloy development for various applications including renewable energy, biomedical, electronics and thermal management. However, further research and analysis will be required regarding microstructural analysis along with cost implications and the antimicrobial and thermal diffusivity and conductivity properties for these novel L-PBF alloys. Furthermore, L-PBF parameter optimisation could offer further

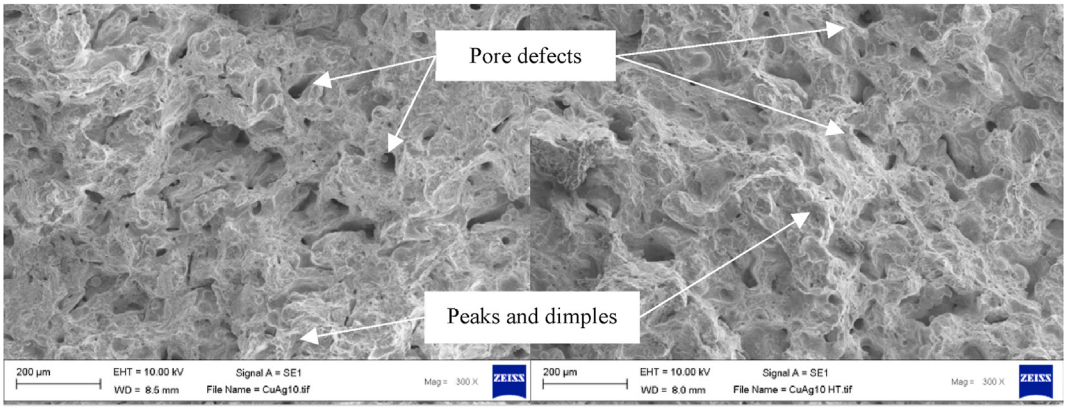

Fig. 18. Scanning Electron Microscopy (SEM) data for CuAg alloy fracture surfaces showing (a) as built CuAg10 and (b) CuAg10 Annealed.

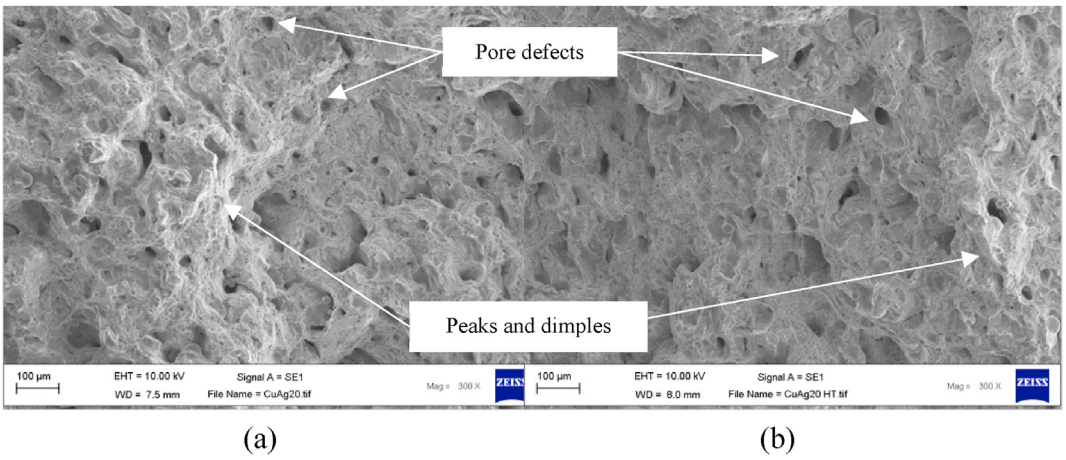

Fig. 19. Scanning Electron Microscopy (SEM) images for CuAg alloy fracture surfaces showing (a) as built CuAg20 (b) CuAg20 Annealed.

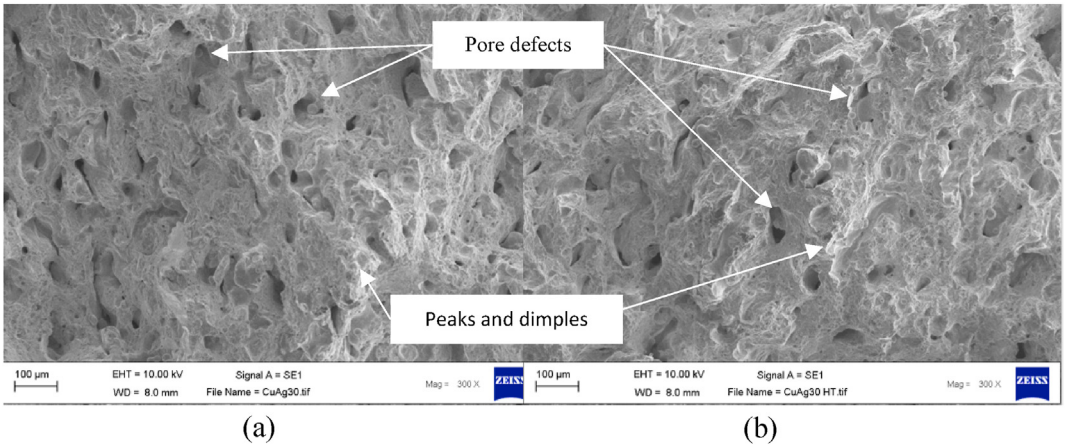

Fig. 20. Scanning Electron Microscopy (SEM) images for CuAg alloy fracture surfaces showing (a) as built CuAg30 (b) CuAg30 annealed.

improvements in achievable properties and therefore future studies would benefit from this analysis. Unfortunately, parameter optimisation could not be included in the scope of this study due to the composition variant and difficulty allocating cause and effect.

5. Conclusions

This study presents CuAg structures with varying Ag content fabricated using the L-PBF in situ alloying. The resultant pore defect distribution, atomic lattice structures and mechanical performance are reported for both as built and annealed conditions. The XCT analysis showed that as Ag content increased both the number of pores and average pore size decrease for both as built and annealed samples. Increasing Ag content from 10% to 30% saw the number of pores decrease by 87% and 83% for as built and annealed samples with average pore size decreasing by 40% and 9.5% respectively. However, the annealing process increased pore content significantly with CuAg10 alloy experiencing a 164% increase between as built and annealed conditions. The subsequent XRD analysis confirmed the presence of a cubic atomic structure where the increase in Ag content increased the atomic d-spacing. This is explained by the inclusion of the relatively large silver atoms within the CuAg atomic lattice structures. However, following the annealing process atomic d-spacing reduced due to atomic lattice contractions. D-spacing reduced by 0.29%, 1.29% and 2.26% respectively for CuAg10, CuAg20

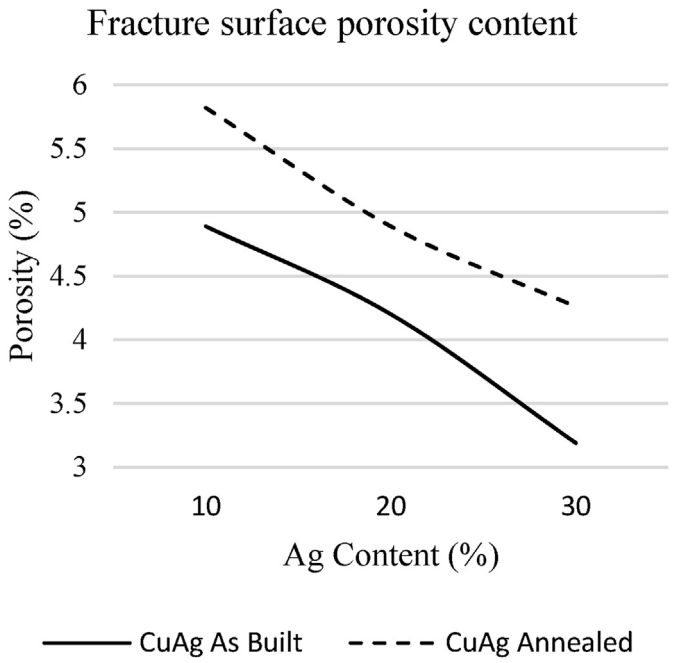

Fig. 21. Influence of Ag addition on fracture surface porosity content of SLM CuAg in situ alloys.

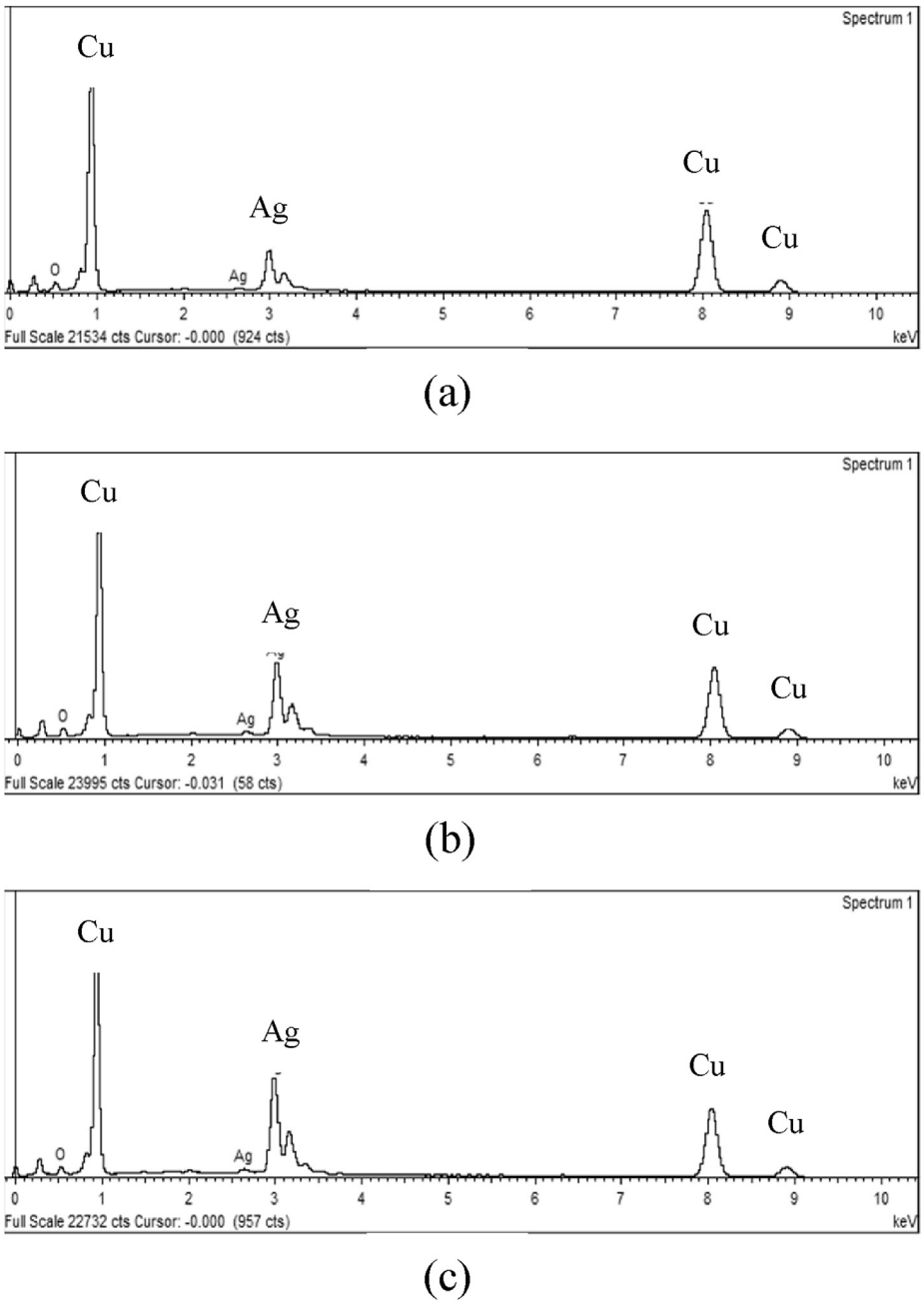

Fig. 22. Energy Dispersive X-Ray (EDX) element analysis for CuAg fracture surfaces (a) CuAg10, (b) CuAg20 and (c) CuAg30.

and CuAg30 following the annealing process. As built d-spacing displayed a 1.93% increase with increased Ag content from CuAg10 to CuAg30 while annealed samples saw a maximum 0.2% change in d-spacing for all three samples. It was also found that the atomic lattice contraction combined with recrystallisation had a significant effect on mechanical performance due to stronger binding effects at the CuAg interfaces reducing dislocation movements. While CuAg10 samples displayed higher yield and ultimate tensile strength than the equivalent annealed samples, CuAg20 showed comparable yield and ultimate tensile strength values for both as built and annealed cases. Nevertheless, as built samples saw an increase in yield strength of 23% and 48% as Ag content increased from 10% to 20% and 20%–30%. Annealed samples saw yield strength increase by 36% and 87% respectively. Similarly, UTS of as built samples saw increases of 22% and 37% while annealed samples increased by 31% and 68%. With increases of 87% (yield strength) and 68% (UTS) for Ag addition at 30%, it is clear the annealing process has a profound effect on material strength for Ag addition of above 20%. When it comes to Youngs modulus Ag increase from CuAg10 to CuAg30 resulted in a 23% and 15% increase for as built samples and 15% and 36% for annealed samples. Evaluating the fracture surfaces revealed that the Ag content was similar to the powder feedstock confirming a homogeneous distribution throughout the L-PBF build and sample fabrication. Although, the SEM analysis of the fracture surfaces showed no visible lack of fusion porosities or unmolten powder some porosity voids were visible. Overall, the SEM data showed that the fracture surface pore content decreased with increase in Ag content.

Table 3
Elemental Ag weight composition of the different CuAg fracture surfaces as informed by the EDX spectrum.

Material	Ag Weight (%)
CuAg10	16.41
CuAg20	29.00
CuAg30	35.42

Data availability

The data that supports the findings of this study are available from the corresponding author upon reasonable request.

CRediT authorship contribution statement

John Robinson: Conceptualisation, Methodology, Software, Investigation, Validation, Formal analysis, Writing - original draft, Writing - review & editing. **Arun Arjunan:** Conceptualisation, Supervision, Methodology, Software, Investigation, Validation, Formal analysis, Writing - original draft, Writing - review & editing. **Mark Stanford:** Conceptualisation, Validation, Formal analysis, Writing - review & editing. **Iain Lyall:** Conceptualisation, Validation, Formal analysis, Writing - review & editing. **Craig Williams:** Conceptualisation, Methodology, Software, Validation, Formal analysis, Writing - review & editing.

Declaration of competing interest

The authors declare that they have no known competing financial interests or personal relationships that could have appeared to influence the work reported in this paper.

Acknowledgements

This research is supported by the University of Wolverhampton and 6Dme Ltd.

References

[1] S. Zhang, H. Zhu, L. Zhang, W. Zhang, H. Yang, X. Zeng, Microstructure and properties of high strength and high conductivity Cu-Cr alloy components fabricated by high power selective laser melting, Mater. Lett. 237 (2019) 306–309, https://doi.org/10.1016/j.matlet.2018.11.118.
[2] C. Silbernagel, L. Gargalis, I. Ashcroft, R. Hague, M. Galea, P. Dickens, Electrical resistivity of pure copper processed by medium-powered laser powder bed fusion additive manufacturing for use in electromagnetic applications, Addit. Manuf. 29 (2019) 100831, https://doi.org/10.1016/j.addma.2019.100831.
[3] R. Bernasconi, J.L. Hart, A.C. Lang, L. Magagnin, L. Nobili, M.L. Taheri, Structural properties of electrodeposited Cu-Ag alloys, Electrochim. Acta 251 (2017) 475–481, https://doi.org/10.1016/j.electacta.2017.08.097.
[4] N. Ciacotich, R.U. Din, J.J. Sloth, P. Møller, L. Gram, An electroplated copper–silver alloy as antibacterial coating on stainless steel, Surf. Coating. Technol. 345 (2018) 96–104, https://doi.org/10.1016/j.surfcoat.2018.04.007.
[5] H. Palza, M. Nuñez, R. Bastías, K. Delgado, In situ antimicrobial behavior of materials with copper-based additives in a hospital environment, Int. J. Antimicrob. Agents 51 (2018) 912–917, https://doi.org/10.1016/j.ijantimicag.2018.02.007.
[6] D. Bradley, Every silver-lined solar cell, Mater. Today 12 (2009) 10, https://doi.org/10.1016/s1369-7021(09)70291-3.
[7] B. Szaraniec, T. Goryczka, Structure and properties of Ti-Ag alloys produced by powder metallurgy, J. Alloys Compd. 709 (2017) 464–472, https://doi.org/10.1016/j.jallcom.2017.03.155.
[8] A. Sun, Z. Wu, X. Dong, B. Duan, D. Wang, Effects of Ag addition on electrical and thermal properties of Mo-Cu composites, J. Alloys Compd. 657 (2016) 8–11, https://doi.org/10.1016/j.jallcom.2015.10.098.
[9] B. Szaraniec, T. Goryczka, Structure and properties of Ti-Ag alloys produced by powder metallurgy, J. Alloys Compd. 709 (2017) 464–472, https://doi.org/10.1016/j.jallcom.2017.03.155.
[10] B.G. Zhang, G.Q. Chen, C.G. Zhang, J.Q. Ni, Structure and mechanical properties of aluminum alloy/Ag interlayer/steel non-centered electron beam welded joints, Trans. Nonferrous Met. Soc. China (English Ed. 21 (2011) 2592–2596, https://doi.org/10.1016/S1003-6326(11)61096-0.
[11] F. Ren, S.N. Arshad, P. Bellon, R.S. Averback, M. Pouryazdan, H. Hahn, Sliding wear-induced chemical nanolayering in Cu-Ag, and its implications for high wear resistance, Acta Mater. 72 (2014) 148–158, https://doi.org/10.1016/j.actamat.2014.03.060.
[12] G. Abbas Gohar, T. Manzoor, A.N. Shah, Investigation of thermal and mechanical properties of Cu-Al alloys with silver addition prepared by powder metallurgy, J. Alloys Compd. 735 (2018) 802–812, https://doi.org/10.1016/j.jallcom.2017.11.176.
[13] M. Wang, R. Li, T. Yuan, C. Chen, M. Zhang, Q. Weng, J. Yuan, Selective laser melting of W-Ni-Cu composite powder: densification, microstructure evolution and nano-crystalline formation, Int. J. Refract. Metals Hard Mater. 70 (2018) 9–18, https://doi.org/10.1016/j.ijrmhm.2017.09.004.
[14] D. Gu, Y. Shen, X. Wu, Formation of a novel W-rim/Cu-core structure during direct laser sintering of W-Cu composite system, Mater. Lett. 62 (2008) 1765–1768, https://doi.org/10.1016/j.matlet.2007.09.087.
[15] D. Gu, Y. Shen, Effects of processing parameters on consolidation and microstructure of W-Cu components by DMLS, J. Alloys Compd. 473 (2009) 107–115, https://doi.org/10.1016/j.jallcom.2008.05.065.
[16] A. Yan, Z. Wang, T. Yang, Y. Wang, Z. Ma, Microstructure, thermal physical property and surface morphology of W-Cu composite fabricated via selective laser melting, Mater. Des. 109 (2016) 79–87, https://doi.org/10.1016/j.matdes.2016.07.049.
[17] K.G. Cooper, J.L. Lydon, M.D. Lecorre, Z.C. Jones, Three-Dimensional Printing GRCop-42, 2019.
[18] S.L. Sing, S. Huang, W.Y. Yeong, Effect of solution heat treatment on microstructure and mechanical properties of laser powder bed fusion produced cobalt-28chromium-6molybdenum, Mater. Sci. Eng. 769 (2020) 138511, https://doi.org/10.1016/j.msea.2019.138511.
[19] D. Jafari, W.W. Wits, The utilization of selective laser melting technology on heat transfer devices for thermal energy conversion applications: a review, Renew. Sustain. Energy Rev. 91 (2018) 420–442, https://doi.org/10.1016/j.rser.2018.03.109.
[20] M.K. Thompson, G. Moroni, T. Vaneker, G. Fadel, R.I. Campbell, I. Gibson, A. Bernard, J. Schulz, P. Graf, B. Ahuja, F. Martina, Design for additive manufacturing: trends, opportunities, considerations, and constraints, CIRP Ann. - Manuf. Technol. 65 (2016) 737–760, https://doi.org/10.1016/j.cirp.2016.05.004.
[21] T.E. Johnson, A.T. Gaynor, Three-dimensional projection-based topology optimization for prescribed-angle self-supporting additively manufactured structures, Addit. Manuf. 24 (2018) 667–686, https://doi.org/10.1016/j.addma.2018.06.011.
[22] S.M. Thompson, Z.S. Aspin, N. Shamsaei, A. Elwany, L. Bian, Additive manufacturing of heat exchangers: a case study on a multi-layered Ti-6Al-4V oscillating heat pipe, Addit. Manuf. 8 (2015) 163–174, https://doi.org/10.1016/j.addma.2015.09.003.
[23] W.H. Yu, S.L. Sing, C.K. Chua, C.N. Kuo, X.L. Tian, Particle-reinforced metal matrix nanocomposites fabricated by selective laser melting: a state of the art review, Prog. Mater. Sci. 104 (2019) 330–379, https://doi.org/10.1016/j.pmatsci.2019.04.006.
[24] S. Dadbakhsh, R. Mertens, L. Hao, J. Van Humbeeck, J.P. Kruth, Selective laser melting to manufacture “in situ” metal matrix composites: a review, Adv. Eng. Mater. 21 (2019) 1–18, https://doi.org/10.1002/adem.201801244.
[25] S. Huang, S.L. Sing, G. de Looze, R. Wilson, W.Y. Yeong, Laser powder bed fusion of titanium-tantalum alloys: compositions and designs for biomedical applications, J. Mech. Behav. Biomed. Mater. 108 (2020) 103775, https://doi.org/10.1016/j.jmbbm.2020.103775.
[26] A.M. Vilardell, I. Yadroitsev, I. Yadroitsava, M. Albu, N. Takata, M. Kobashi, P. Krakhmalev, D. Kouprianoff, G. Kothleitner, A. du Plessis, Manufacturing and characterization of in-situ alloyed Ti6Al4V(ELI)-3 at.% Cu by laser powder bed fusion, Addit. Manuf. 36 (2020), https://doi.org/10.1016/j.addma.2020.101436.
[27] T. Hanemann, L.N. Carter, M. Habschied, N.J.E. Adkins, M.M. Attallah, M. Heilmaier, In-situ alloying of AlSi10Mg+Si using Selective Laser Melting to control the coefficient of thermal expansion, J. Alloys Compd. 795 (2019) 8–18, https://doi.org/10.1016/j.jallcom.2019.04.260.
[28] S. Huang, S.L. Sing, G. de Looze, R. Wilson, W.Y. Yeong, Laser powder bed fusion of titanium-tantalum alloys: compositions and designs for biomedical applications, J. Mech. Behav. Biomed. Mater. 108 (2020) 103775, https://doi.org/10.1016/j.jmbbm.2020.103775.
[29] R. Martinez, I. Todd, K. Mumtaz, In situ alloying of elemental Al-Cu12 feedstock using selective laser melting, Virtual Phys. Prototyp. 14 (2019) 242–252, https://doi.org/10.1080/17452759.2019.1584402.
[30] P. O'Regan, P. Prickett, R. Setchi, G. Hankins, N. Jones, Metal based additive layer manufacturing: variations, correlations and process control, Procedia Comput. Sci. 96 (2016) 216–224, https://doi.org/10.1016/j.procs.2016.08.134.
[31] I. Yadroitsev, A. Gusarov, I. Yadroitsava, I. Smurov, Single track formation in selective laser melting of metal powders, J. Mater. Process. Technol. 210 (2010) 1624–1631, https://doi.org/10.1016/j.jmatprotec.2010.05.010.
[32] A. Gisario, M. Barletta, R. Stancampiano, On the interaction mechanisms between a high-power diode laser source and silver alloys: the case of aesthetic welding, Optic Laser. Eng. 47 (2009) 821–830, https://doi.org/10.1016/j.optlaseng.2009.02.003.

[33] W. Xiong, L. Hao, Y. Li, D. Tang, Q. Cui, Z. Feng, C. Yan, Effect of selective laser melting parameters on morphology, microstructure, densification and mechanical properties of supersaturated silver alloy, Mater. Des. 170 (2019) 107697, https://doi.org/10.1016/j.matdes.2019.107697.
[34] C.P. Wu, D.Q. Yi, W. Weng, S.H. Li, J.M. Zhou, Influence of alloy components on arc erosion morphology of Ag/MeO electrical contact materials, Trans. Nonferrous Met. Soc. China (English Ed. 26 (2016) 185−195, https://doi.org/10.1016/S1003-6326(16)64105-5.
[35] S. Maharubin, Y. Hu, D. Sooriyaarachchi, W. Cong, G.Z. Tan, Laser engineered net shaping of antimicrobial and biocompatible titanium-silver alloys, Mater. Sci. Eng. C 105 (2019) 110059, https://doi.org/10.1016/j.msec.2019.110059.
[36] M. Bayat, A. Thanki, S. Mohanty, A. Witvrouw, S. Yang, J. Thorborg, N.S. Tiedje, J.H. Hattel, Keyhole-induced porosities in laser-based powder bed fusion (L-PBF) of Ti6Al4V: high-fidelity modelling and experimental validation, Addit. Manuf. 30 (2019) 100835, https://doi.org/10.1016/j.addma.2019.100835.
[37] W. Yu, S.L. Sing, C.K. Chua, X. Tian, Influence of re-melting on surface roughness and porosity of AlSi10Mg parts fabricated by selective laser melting, J. Alloys Compd. 792 (2019) 574−581, https://doi.org/10.1016/j.jallcom.2019.04.017.
[38] F.H. Kim, S.P. Moylan, E.J. Garboczi, J.A. Slotwinski, Investigation of pore structure in cobalt chrome additively manufactured parts using X-ray computed tomography and three-dimensional image analysis, Addit. Manuf. 17 (2017) 23−38, https://doi.org/10.1016/j.addma.2017.06.011.
[39] B. Zhang, S. Liu, Y.C. Shin, In-Process monitoring of porosity during laser additive manufacturing process, Addit. Manuf. 28 (2019) 497−505, https://doi.org/10.1016/j.addma.2019.05.030.
[40] J. Robinson, M. Stanford, A. Arjunan, Stable formation of powder bed laser fused 99.9% silver, Mater. Today Commun. 24 (2020) 101195, https://doi.org/10.1016/j.mtcomm.2020.101195.
[41] H. Lee, J.H.J. Kim, J.H. Moon, W.W. Kim, E.A. Seo, Correlation between pore characteristics and tensile bond strength of additive manufactured mortar using X-ray computed tomography, Construct. Build. Mater. 226 (2019) 712−720, https://doi.org/10.1016/j.conbuildmat.2019.07.161.
[42] J. Fieres, P. Schumann, C. Reinhart, Predicting failure in additively manufactured parts using X-ray computed tomography and simulation, Procedia Eng 213 (2018) 69−78, https://doi.org/10.1016/j.proeng.2018.02.008.
[43] J.H. Tan, W.L.E. Wong, K.W. Dalgarno, An overview of powder granulometry on feedstock and part performance in the selective laser melting process, Addit. Manuf. 18 (2017) 228−255, https://doi.org/10.1016/j.addma.2017.10.011.
[44] C. Pleass, S. Jothi, Influence of powder characteristics and additive manufacturing process parameters on the microstructure and mechanical behaviour of Inconel 625 fabricated by Selective Laser Melting, Addit. Manuf. 24 (2018) 419−431, https://doi.org/10.1016/j.addma.2018.09.023.
[45] Shannon L. Taylor (2013). An Investigation of the Mechanical and Physical Properties of Copper-Silver Alloys and the Use of These Alloys in Pre-Columbian America. https://www.researchgate.net/publication/279814785_An_investigation_of_the_mechanical_and_physical_properties_of_copper-silver_alloys_and_the_use_of_these_alloys_in_Pre-Columbian_America.
[46] A. Tridello, J. Fiocchi, C.A. Biffi, G. Chiandussi, M. Rossetto, A. Tuissi, D.S. Paolino, VHCF response of Gaussian SLM AlSi10Mg specimens: effect of a stress relief heat treatment, Int. J. Fatig. 124 (2019) 435−443, https://doi.org/10.1016/j.ijfatigue.2019.02.020.
[47] M. Frkan, R. Konecna, G. Nicoletto, L. Kunz, Microstructure and fatigue performance of SLM-fabricated Ti6Al4V alloy after different stress-relief heat treatments, Transp. Res. Procedia. 40 (2019) 24−29, https://doi.org/10.1016/j.trpro.2019.07.005.
[48] E. Liverani, S. Toschi, L. Ceschini, A. Fortunato, Effect of selective laser melting (SLM) process parameters on microstructure and mechanical properties of 316L austenitic stainless steel, J. Mater. Process. Technol. 249 (2017) 255−263, https://doi.org/10.1016/j.jmatprotec.2017.05.042.
[49] N. Ortega, S. Martínez, I. Cerrillo, A. Lamikiz, E. Ukar, Computed tomography approach to quality control of the Inconel 718 components obtained by additive manufacturing (SLM), Procedia Manuf 13 (2017) 116−123, https://doi.org/10.1016/j.promfg.2017.09.018.
[50] M. Bayat, A. Thanki, S. Mohanty, A. Witvrouw, S. Yang, J. Thorborg, N. Skat Tiedje, J.H. Hattel, Keyhole-induced porosities in laser-based powder bed fusion (L-PBF) of Ti6Al4V: high-fidelity modelling and experimental validation, Addit. Manuf. (2019) 100835, https://doi.org/10.1016/j.addma.2019.100835.
[51] L. Yang, L. Chen, Y.C. Chen, L. Kang, J. Yu, Y. Wang, C. Lu, T. Mashimo, A. Yoshiasa, C.H. Lin, Homogeneously alloyed nanoparticles of immiscible Ag−Cu with ultrahigh antibacterial activity, Colloids Surf. B Biointerfaces 180 (2019) 466−472, https://doi.org/10.1016/j.colsurfb.2019.05.018.
[52] B. Mouffok, H. Feraoun, H. Aourag, Vacancy effect in CuAg alloys, Mater. Lett. 60 (2006) 1344−1346, https://doi.org/10.1016/j.matlet.2005.11.026.
[53] H. Feraoun, H. Aourag, T. Grosdidier, D. Klein, C. Coddet, Development of modified embedded atom potentials for the Cu-Ag system, Superlattice. Microst. 30 (2001) 261−271, https://doi.org/10.1006/spmi.2002.1016.
[54] H. Feraoun, C. Esling, L. Dembinski, T. Grosdidier, C. Coddet, H. Aourag, A new form of the Sutton-Chen potential for the Cu-Ag alloys, Superlattice. Microst. 31 (2002) 297−313, https://doi.org/10.1006/spmi.2002.1049.
[55] S. Abdeslam, Influence of silver inclusions on the mechanical behavior of Cu-Ag nanocomposite during nanoindentation: molecular dynamics study, Results Phys 15 (2019) 102672, https://doi.org/10.1016/j.rinp.2019.102672.
[56] C. Paper, T.D. Panalytical, Use of Cluster Analysis of XRD Data for Ore Evaluation Accuracy in Powder Diffraction IV NIST, USA Uwe König Thomas Degen PANalytical B . V . Almelo, Gaithersburg MD, 2015. The Netherlands,.
[57] Y. Champion, J. Bourgon, X. Sauvage, Modified strain rate regime in ultrafine grained copper with silver micro-alloying, Mater. Sci. Eng. 657 (2016) 1−5, https://doi.org/10.1016/j.msea.2016.01.044.
[58] H. Zhao, H. Fu, M. Xie, J. Xie, Effect of Ag content and drawing strain on microstructure and properties of directionally solidified Cu-Ag alloy, Vacuum 154 (2018) 190−199, https://doi.org/10.1016/j.vacuum.2018.05.010.